Catalysis Science & Technology

PAPER

View Article Online
View Journal

Cite this: DOI: 10.1039/c9cy01385g

Effect of perimeter interface length between 2D WO_3 monolayer domain and γ-Al_2O_3 on selective hydrogenolysis of glycerol to 1,3-propanediol†

Takeshi Aihara,[a] Hiroki Miura [abd] and Tetsuya Shishido *[abcd]

Received 14th July 2019,
Accepted 4th September 2019

DOI: 10.1039/c9cy01385g

rsc.li/catalysis

The relationship between the structure of W species on Pt/WO_3/Al_2O_3 catalysts and their activity for selective hydrogenolysis of glycerol to 1,3-propanediol was investigated. Structural analysis by spectroscopic techniques including X-ray diffraction (XRD), X-ray photoelectron spectroscopy (XPS) and X-ray adsorption fine structure (XAFS) revealed the formation of two-dimensional WO_3 monolayer domains on the surface of γ-Al_2O_3 at a WO_3 loading level of below 20 wt%. Evaluation of the reduction properties of W species by H_2 temperature programed reduction (TPR) suggested the presence of two kinds of W species with different reduction properties loaded on γ-Al_2O_3, and W species at the edge of a WO_3 domain was reduced more easily than that inside of a WO_3 domain. Furthermore, the length of the perimeter interface between a two-dimensional WO_3 monolayer domain and γ-Al_2O_3 (W–Al perimeter interface) could be estimated from the difference in their reducibility. The positive correlation between W–Al perimeter interface length and the yield of 1,3-propanediol in hydrogenolysis of glycerol indicated that a W–(OH)–Al site at the W–Al perimeter interface functioned as a main active site.

Introduction

It is important to elucidate the detailed relationship between the structures of catalysts and their catalytic performance to establish guidelines for designing highly active catalysts.[1–4] Supported group V–VII metal oxides are widely used as catalysts in oil refinery, biomass conversion and selective catalytic reduction (SCR) of NO_x.[5–10] The boundaries between different metal oxides often exhibit unique catalytic properties that are not observed in the simple metal oxide. Iglesia and coworkers investigated the relationship between the structures of WO_x species on ZrO_2 and their catalytic activities for *o*-xylene isomerization,[11–13] in which the domain size of WO_x dominated the acid properties of the catalyst.[14–16] Wachs and coworkers proposed the importance of a Brønsted acid site generated at the boundary between a supported metal oxide and the support,[17,18] and insisted that their acidic properties were strongly affected by the structure of the catalyst.[19–25] Previously, we found that supported Group V–VI metal oxides (Nb, Ta, Mo, and W) on γ-Al_2O_3 exhibited the greatest Brønsted acidity when the γ-Al_2O_3 surface was almost fully covered with these metal oxides as a two-dimensional (2D) monolayer.[26–34]

On the other hand, hydrogenolysis is one of the most useful reactions for producing value-added products from biomass-derived compounds.[35–38] Particularly, highly efficient and selective hydrogenolysis of the C–O bond at the second position of glycerol is of great importance, since this can provide 1,3-propanediol, which is a useful monomer for polytrimethylene terephthalate (PTT) resin.[39–43] The efficient catalysis by tungsten oxide with Pt for the hydrogenolysis of glycerol to 1,3-propanediol has been reported.[44–49] Recently, we reported that the surface coverage of a 2D WO_3 monolayer on a metal–oxide support significantly affected the activity of supported Pt/WO_3 catalysts for the selective hydrogenolysis of biomass compounds,[50,51] and proposed that the perimeter interface between WO_3 and γ-Al_2O_3 played an important role in the selective formation of 1,3-propandiol from glycerol.[50] However, the detailed role of tungsten species in catalytic hydrogenolysis is still under discussion due to the difficulty of evaluating the structure of the perimeter interface between different metal–oxides. Despite the fact that microscopic analyses such as transmission electron microscopy (TEM),[52–54] scanning electron microscopy (SEM)[55] and scanning tunneling microscopy (STM)[56,57] are often used to observe the interfacial length or size of metal or metal oxides,

[a] *Department of Applied Chemistry for Environment, Graduate School of Urban Environmental Sciences, Tokyo Metropolitan University, 1-1 Minami-Osawa, Hachioji, Tokyo 192-0397, Japan. E-mail: shishido-tetsuya@tmu.ac.jp*
[b] *Research Center for Hydrogen Energy-based Society, Tokyo Metropolitan University, 1-1 Minami-Osawa, Hachioji, Tokyo 192-0397, Japan*
[c] *Research Center for Gold Chemistry, Tokyo Metropolitan University, 1-1 Minami-Osawa, Hachioji, Tokyo 192-0397, Japan*
[d] *Elements Strategy Initiative for Catalysts & Batteries, Kyoto University, Katsura, Nishikyo-ku, Kyoto 615-8520, Japan*
† Electronic supplementary information (ESI) available. See DOI: 10.1039/c9cy01385g

these techniques have hardly been used to observe the boundary between a supported metal oxide and the support due to slight differences in their contrasting density. Hence, the development of novel techniques to estimate the length of the perimeter interface between two kinds of metal oxides would be useful for controlling the structure and catalytic activity.

Herein, we investigated the relationship between the length of the perimeter interface between WO_3 and γ-Al_2O_3 (W–Al perimeter interface) and the catalytic activity for hydrogenolysis of glycerol to 1,3-propanediol over $Pt/WO_3/Al_2O_3$ catalysts. The detailed characterization of the structure and reducibility of W species on $Pt/WO_3/Al_2O_3$ catalysts enabled us to evaluate the length of the W–Al perimeter interface, which supports the notion that the perimeter interface plays an important role in the hydrogenolysis of glycerol to 1,3-propanediol.

Experimental

Materials

H_2PtCl_6 and $(NH_4)_{10}W_{12}O_{42}{\cdot}5H_2O$ were purchased from FURUYA METAL Co. Ltd and Wako Chemicals, respectively. γ-Al_2O_3 (Sumitomo Chemical Co., Ltd, AKP-G015; JRC-ALO-8 equivalent) was obtained from the Catalysis Society of Japan. $PtCl_2$ was purchased from Aldrich. $PtCl_4$ and PtO_2 were purchased from Wako Chemicals. For the reference sample for XAFS analysis, Na_2WO_4 and WO_3 were purchased from Wako Chemicals. Ba_2NiWO_6 was synthesized by the solid-state reaction from $BaCO_3$, $NiCO_3$ (Wako Chemicals) and WO_3 as described in a previous report.[58]

Preparation of $Pt/WO_3/Al_2O_3$ catalysts

A series of WO_3/Al_2O_3 catalysts was prepared by impregnation of γ-Al_2O_3 with an aqueous solution of $(NH_4)_{10}W_{12}O_{42}{\cdot}5H_2O$ at 353 K for 2 h, dried at 353 K for 6 h, and then calcined at 1123 K for 3 h in flowing air.[34] $Pt/WO_3/Al_2O_3$ catalysts (Pt loading: 1 wt%) were also prepared by impregnating WO_3/Al_2O_3 with an aqueous solution of H_2PtCl_6 for 2 h and dried at 353 K for 6 h. After the impregnation procedure, the prepared catalysts were calcined at 573 K for 3 h in air.

Procedure for hydrogenolysis

The hydrogenolysis of glycerol was carried out in a Teflon vessel placed in a 50 mL stainless steel autoclave. Three mmol of glycerol and 100 mg of a catalyst together with 9 mL of H_2O were added to the reactor. After the reactors were sealed, their air was purged by hydrogen and the reactors were pressurized to 5 MPa. The reaction was carried out at 453 K for 15 h.

Physical and analytical measurement

The products of the catalytic runs were analyzed by gas chromatography (Shimadzu GC-2014 equipped with a flame ionization detector, Stabilwax capillary column, i.d. 0.53 mm, length 30 m, 80–250 °C). X-ray diffraction (XRD) patterns of the catalyst were recorded by Rigaku SmartLab with Cu Kαradiation. The samples were scanned from 2θ = 10–70 degrees at 10 degrees min^{-1} and a resolution of 0.01 degrees. X-ray photoelectron spectroscopy (XPS) analysis of the catalysts was performed using a JEOL JPS-9010 MX instrument. The spectra were measured using Mg Kα radiation. All spectra were calibrated using C 1s (284.5 eV) as a reference. The Brunauer–Emmett–Teller (BET) specific surface area was estimated from N_2 isotherms obtained using a BELSORP-mini II (BEL Japan, Osaka, Japan) at 77 K. The analyzed samples were evacuated at 573 K for 3 h prior to the measurement. X-ray absorption spectroscopy (XAS) analysis of the catalysts was performed at the BL01B1 beamline at SPring-8 (Hyogo, Japan). The ring energy was 8 GeV, and the stored current was 99.5 mA. W L_3-edge (10.2 keV) and W L_1-edge (12.1 keV) X-ray absorption spectra were recorded by using Si(311) and Si(111) crystal monochromators, respectively. All spectra were obtained in transmission mode. Data reduction was performed by using xTunes (Science & Technology Inst., Co.).[59] The pre-edge peak areas of W L_1-edge XANES spectra were estimated by the deconvolution of spectra with one or two Lorenz functions and one arctangent function. Temperature programmed reduction (H_2-TPR) was also carried out in an Okura BP-2 instrument equipped with TCD for determination of H_2 consumption and molecular sieve 4 Å traps to remove the water formed during reduction. H_2-TPR profiles of each catalyst (30 mg) were recorded from 323 K to 1273 K at 10 K min^{-1} under 5% H_2/Ar flowing at 30 mL min^{-1}.

Results and discussion

Glycerol hydrogenolysis was carried out over $Pt/WO_3/Al_2O_3$ catalysts with various WO_3 loadings (Scheme 1 and Fig. S1†). Although Pt/Al_2O_3 catalyst was not effective for the reaction, the loading of WO_3 enabled cleavage of the C–O bond at the second position of glycerol selectively to give 1,3-propanediol (Fig. 1). The loading amount of WO_3 on γ-Al_2O_3 remarkably affected the yield of the product, and the yield increased with increasing WO_3 loading; $Pt/WO_3/Al_2O_3$ catalyst with 6 wt% WO_3 loading showed the highest yield of the product. On the other hand, excess loading of WO_3 drastically decreased the catalytic activity of $Pt/WO_3/Al_2O_3$ catalysts, and catalysts with over 20% WO_3 loading showed no activity for the present reaction. These results suggest that the structure of WO_3 on γ-Al_2O_3 should be a dominant factor for determining the catalytic performance in the selective hydrogenolysis of glycerol to 1,3-propanediol. The surface acidity of $Pt/WO_3/Al_2O_3$ catalysts before and after reaction investigated by the NH_3-TPD and pyridine adsorbed IR (Fig. S2†). No change in the acidity on $Pt/WO_3/Al_2O_3$ catalysts before and after the reaction was observed, indicating that the acidity of catalysts was not directly collated to the activity of hydrogenolysis of glycerol to 1,3-propanediol. Although the location of Pt was investigated

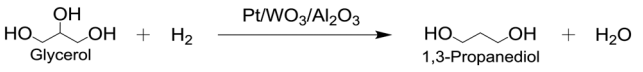

Scheme 1 Hydrogenolysis of glycerol to 1,3-propanediol.

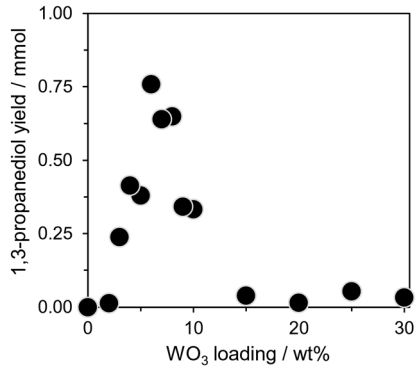

Fig. 1 Effect of WO_3 loading on glycerol hydrogenolysis over $Pt/WO_3/Al_2O_3$ catalysts. Conditions: glycerol (3 mmol), catalyst (100 mg), H_2O (9 mL), P_{H_2} = 5 MPa, T = 453 K, t = 15 h.

by TEM technique, the identification between of Pt and W species was hard due to closeness their atomic number. The location of Pt is currently underway in our laboratory. Dispersity of Pt species on support with various WO_3 loadings was estimated by CO chemisorption. Loading amount of WO_3 did not affect the Pt dispersion, and no clear correlation between Pt dispersion and catalytic activity was observed (Fig. S3†). These results indicate that the location of Pt is not dominant factor for the hydrogenolysis over $Pt/WO_3/Al_2O_3$ catalysts. Hence, in the following section, we focus on elucidation of the relationship between catalytic performance and the structure of W species on the basis of spectroscopic and kinetic characterization of the catalysts.

XRD patterns of $Pt/WO_3/Al_2O_3$ catalysts with various WO_3 loadings are shown in Fig. 2. Diffraction peaks due to crystalline γ-Al_2O_3 were observed in all catalysts. In contrast, peaks attributed to crystalline WO_3 (monoclinic WO_3 (*m*-WO_3) and $Al_2(WO_3)_4$) were found in the catalyst with greater than 20 wt% WO_3 loading. Moreover, no diffraction peaks corresponding to Pt were confirmed for any of the catalysts. These results indicate that amorphous WO_3 is loaded on the surface of γ-Al_2O_3 of the catalysts with below 20 wt% WO_3 loading, and Pt species is highly dispersed on the WO_3/Al_2O_3 surface. No diffraction peaks corresponding to Pt were confirmed for any of the catalysts. Moreover, no clear WO_3 particles were observed in a TEM image of WO_3/Al_2O_3 catalyst with 7 wt% WO_3 loading (Fig. S4†). The location of Pt was also investigated by TEM technique. However, it was quite difficult to distinguish whether Pt nanoparticles were distributed on either the WO_3 monolayer or γ-Al_2O_3, because their atomic numbers of Pt and W are close each other.

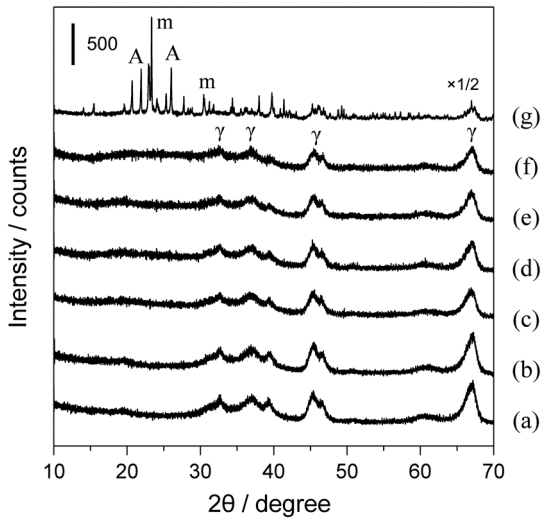

Fig. 2 XRD patterns of $Pt/WO_3/Al_2O_3$ catalysts with various WO_3 loadings. (a) 0, (b) 2, (c) 6, (d) 10, (e) 15, (f) 20 and (g) 30 wt%. γ: γ-Al_2O_3, *m*: *m*-WO_3, A: $Al_2(WO_4)_3$.

XP spectra of $Pt/WO_3/Al_2O_3$ catalysts with various WO_3 loadings are shown in Fig. S5.† The peaks due to W $4f_{7/2}$ and W $4f_{5/2}$ appeared at 36.0 and 38.1 eV, respectively. These peak positions were constant regardless of the Pt and WO_3 loading of the catalysts, indicating that W^{6+} species[60,61] is present on all the catalysts. The surface W/Al atomic ratio on the catalysts was also estimated on the basis of the areas of the W 4f and Al 2p peaks in the XP spectra (Fig. 3). The surface W/Al ratio of $Pt/WO_3/Al_2O_3$ catalysts increased linearly with WO_3 loading up to 20 wt%, and then increased gradually. The same tendency was observed in the case of WO_3/Al_2O_3. These results indicate that the state of the tungsten species loaded on the surface of the catalysts changes at 20 wt% WO_3 loading regardless of the presence of Pt species. The density of surface tungsten species on the catalyst with 20 wt% WO_3 loading was estimated to be 4.5 W atoms nm^{-2}. Previous literature reported that the tungsten density is around 4.0 atoms nm^{-2} when the WO_3 monolayer fully covers the surface of Al_2O_3.[24,62] This value is comparable to our estimated value, indicating that WO_3 is loaded as a 2D monolayer on γ-Al_2O_3 at a WO_3 loading level of less than 20 wt%.

Fig. 4 shows the W L_3-edge k^3-weighted extended X-ray absorption fine structure (EXAFS) oscillations of $Pt/WO_3/Al_2O_3$ catalysts with various WO_3 loadings as well as reference samples. No significant differences were noted in the shapes of the EXAFS oscillations of catalysts with WO_3 loading below 20 wt%. In contrast, the shape of the EXAFS oscillations of $Pt/WO_3/Al_2O_3$ catalysts with 30 wt% loading in the range of 3–5 $Å^{-1}$ clearly resembles that of *m*-WO_3. This result indicates

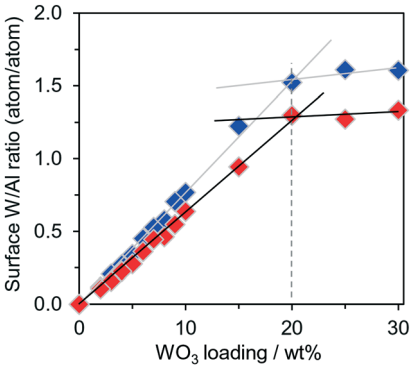

Fig. 3 Surface W/Al ratio of $Pt/WO_3/Al_2O_3$ (◆) and WO_3/Al_2O_3 (◆) catalysts with various WO_3 loadings.

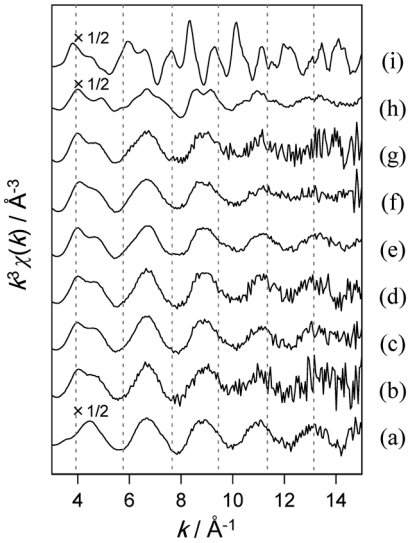

Fig. 4 W L_3-edge EXAFS oscillations of $Pt/WO_3/Al_2O_3$ catalysts with various WO_3 loadings and reference samples. (a) Na_2WO_4, (b) 2, (c) 6, (d) 10, (e) 15, (f) 20, (g) 30 wt%, (h) *m*-WO_3 and (i) Ba_2NiWO_6.

that crystalline WO_3 is formed on the catalyst above 20 wt% WO_3 loading. W L_3-edge Fourier-transformed EXAFS oscillations of $Pt/WO_3/Al_2O_3$ catalysts with various WO_3 loadings and reference samples are shown in Fig. 5. In the spectra of the catalysts with less than 20 wt% WO_3 loading, only a peak at 1–2 Å corresponding to W–O linkage was observed, which indicates that two-dimensional WO_3 monolayer domains were formed on the catalyst surface with WO_3 loading of less than 20 wt%. In contrast, the peak at 3–4 Å, which is attributable to W–O–W linkage, was observed only for $Pt/WO_3/Al_2O_3$ catalyst with 30 wt% loading, implying the generation of crystalline WO_3. These results suggest that 2D WO_3 monolayer

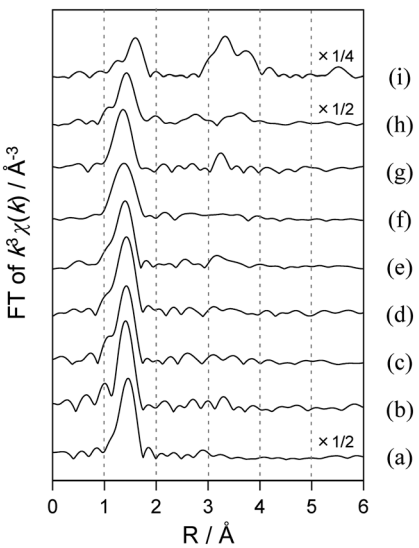

Fig. 5 Fourier-transformed W L_3-edge EXAFS oscillations of $Pt/WO_3/Al_2O_3$ catalysts with various WO_3 loadings and reference samples. (a) Na_2WO_4, (b) 2, (c) 6, (d) 10, (e) 15, (f) 20, (g) 30 wt%, (h) *m*-WO_3 and (i) Ba_2NiWO_6.

domains were loaded on the catalyst surface at up to 20 wt% WO_3 loading.

To obtain more detailed information about the local structure of tungsten species, W L_1-edge XANES spectra of $Pt/WO_3/Al_2O_3$ catalysts with various WO_3 loadings and reference samples were examined (Fig. 6). The pre-edge peak of W L_1-edge XANES is attributed to the electron transition from 2 s to d–p orbitals[63–65] and the local symmetry of tungsten species can be estimated from the area of the pre-edge peak. W species with low symmetry exhibit a larger pre-edge peak area than that with high symmetry.[66,67] The pre-edge peak area of $Pt/WO_3/Al_2O_3$ catalysts and reference samples was estimated by deconvolution of the W L_1-edge XANES spectra with one or two Lorenz functions and an arctangent function (Fig. S6†). The local W symmetry of Na_2WO_4, *m*-WO_3 and Ba_2NiWO_6 is tetrahedral (T_d), distorted octahedral (O_h) and octahedral (D_2), respectively.[66] The pre-edge peak area of reference samples decreased with an increase in the local symmetry of tungsten species (Fig. 7). $Pt/WO_3/Al_2O_3$ catalyst with 2 wt% WO_3 loading showed the largest pre-edge peak area among the series of WO_3-loaded catalysts. The pre-edge peak area of $Pt/WO_3/Al_2O_3$ catalysts decreased with increasing WO_3 loading and the area of 30 wt% WO_3 loading catalyst was comparable to that of *m*-WO_3 with O_h symmetry. These results implied that isolated T_d-symmetric tungsten species was mainly formed on the catalyst with 2 wt% WO_3 loading and the ratio of tungsten species with distorted O_h symmetry to that with T_d symmetry increased with an increase in WO_3 loading. On the other hand, W species in the $Pt/WO_3/Al_2O_3$ catalyst with 30 wt% WO_3 loading showed high O_h symmetry.

To understand the electronic state of Pt loaded on WO_3/Al_2O_3 catalysts, XP spectra in Pt $4d_{5/2}$ and $4d_{3/2}$ were investigated (Fig. 8). The binding energies of $PtCl_2$ were 316.3 and 333.1 eV, respectively. The binding energies of $PtCl_4$ and PtO_2 were 317.8 and 334.7 eV, respectively. The binding energies of $Pt/WO_3/Al_2O_3$ catalysts were 316.0 and 332.9 eV, respectively. No difference in binding energy was observed in the spectra of $Pt/WO_3/Al_2O_3$ catalysts with various WO_3 loadings. These results indicated that the valence of Pt loaded on the WO_3/Al_2O_3 catalysts was almost +2 regardless of the loading amount of WO_3.

The reduction properties of $Pt/WO_3/Al_2O_3$ catalysts with various WO_3 loadings were evaluated by H_2-TPR (Fig. 9). While no reduction peak was confirmed for WO_3/Al_2O_3 catalysts, H_2 consumption was observed in the profiles of all the Pt-loaded catalysts. The fact of H_2-TPR in which Pt promoted the reduction of W species suggests that Pt nanoparticles were loaded on or around the W species (Pt nanoparticles may interact with W species). The investigation of the location of Pt is currently underway in our laboratory. The H_2 consumption peak at around 523 K was observed in the profile of Pt/Al_2O_3 catalyst. Reduction of Pt^{2+} species to Pt metal was reported to occur under 573 K.[68,69] Therefore, the peak observed at around 523 K in Pt/Al_2O_3 catalyst could be attributed to the reduction of Pt^{2+} to Pt^0 species. Moreover, the H_2 consumption peak at around 373–573 K was strongly affected

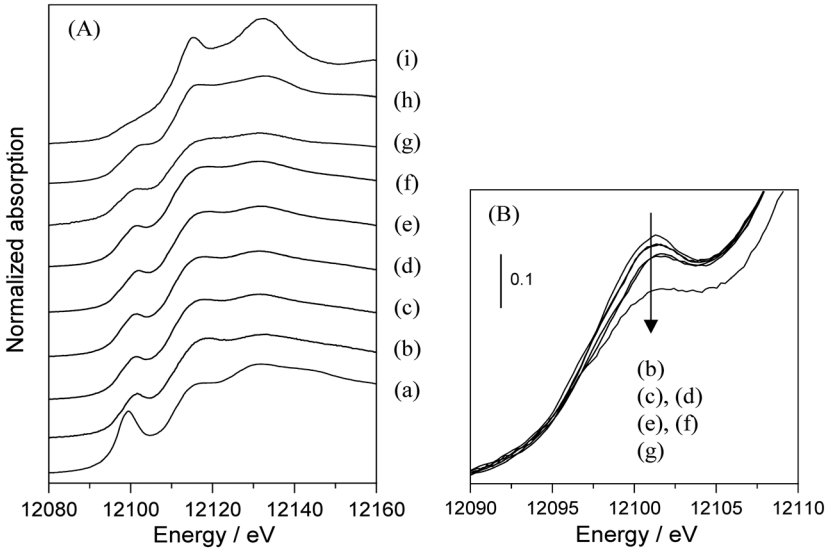

Fig. 6 (A) W L_1-edge XANES spectra of $Pt/WO_3/Al_2O_3$ catalysts with various WO_3 loadings and reference samples. (B) Pre-edge region of W L_1-edge XANES. (a) Na_2WO_4, (b) 2, (c) 6, (d) 10, (e) 15, (f) 20, (g) 30 wt%, (h) *m*-WO_3 and (i) Ba_2NiWO_6.

by the Pt loading. Iglesia and coworkers also reported that the addition of Pt promoted the reduction of tungsten species to consume H_2 at around 373–573 K.[15,70,71] A small WO_3 domain was reported to be reduced at higher temperature than a large WO_3 domain or bulk WO_3.[15,72] The position of the H_2 consumption peak shifted to a lower temperature with an increase in WO_3 loading. This result indicated that the size of the WO_3 domain on the γ-Al_2O_3 surface increased with an increase in WO_3 loading. No remarkable peak shift was observed at the region of W $4f_{7/2}$ and $4f_{5/2}$ in the XP spectra of $Pt/WO_3/Al_2O_3$ catalysts reduced at 453 and 573 K (Fig. S7†). This is probably due to a small fraction of reduced W species in WO_3 domain.

The amounts of H_2 consumption estimated from the peak area of each TPR profile of the catalysts are summarized in Fig. 10(A). The estimated H_2 consumption of Pt/Al_2O_3 catalyst was 45 μmol g^{-1}, which is almost the same as the theoretical value of H_2 consumption (51 μmol g^{-1}) during the reduction of Pt^{2+} to Pt^0. These results suggest that the reduction peak in the TPR profile of Pt/Al_2O_3 catalyst should be due to the reduction of Pt^{2+} to Pt^0. In contrast, the amount of H_2 consumption of $Pt/WO_3/Al_2O_3$ catalysts was greater than that of Pt/Al_2O_3 catalyst. These results imply that the H_2 consumption peak below 673 K includes the reduction of tungsten oxides in addition to the reduction of Pt species. The amount of H_2 consumption due to WO_3 at each catalyst with A wt% WO_3 loading ($X(A)W\cdots X(A)_{WO_3}$) can be calculated as (1)

$$X(A)_{WO_3} = X(A)_{Total} - X_{Pt} \quad (1)$$

$X(A)_{Total}$ represents the total amount of H_2 consumption of the sample with A wt% WO_3 loading and X_{Pt} indicates the

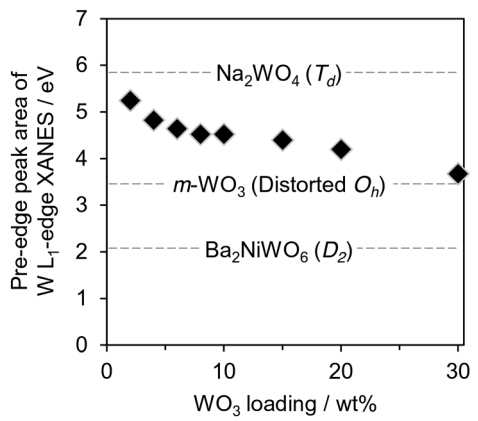

Fig. 7 Pre-edge area of W L_1-edge XANES of $Pt/WO_3/Al_2O_3$ catalysts with various WO_3 loadings.

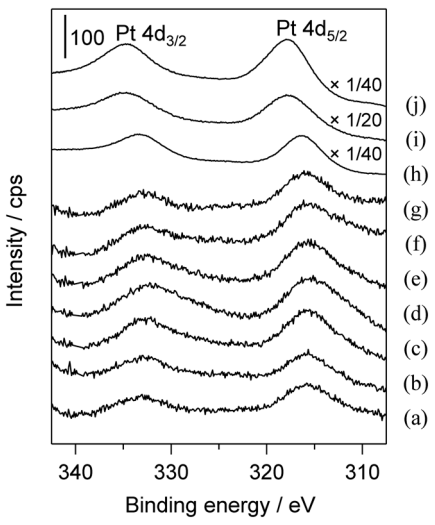

Fig. 8 XP spectra of $Pt/WO_3/Al_2O_3$ catalysts with various WO_3 loadings and reference samples in the Pt 4d region. (a) 0, (b) 2, (c) 6, (d) 10, (e) 15, (f) 20, (g) 30 wt%, (h) $PtCl_2$, (i) $PtCl_4$ and (j) PtO_2.

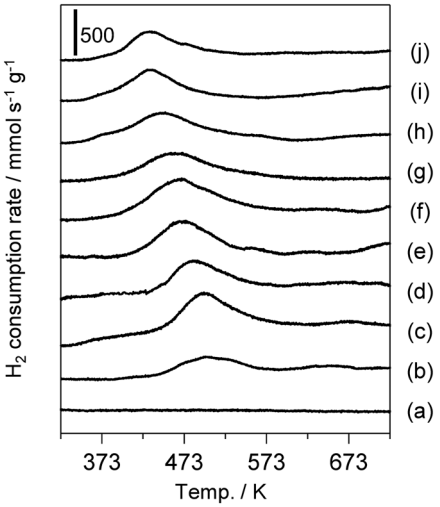

Fig. 9 H_2-TPR profiles of $Pt/WO_3/Al_2O_3$ catalysts with various WO_3 loadings. (a) 6 wt% WO_3/Al_2O_3 (b) 0, (c) 2, (d) 4, (e) 6, (f) 8, (g) 10, (h) 15, (i) 20 and (j) 30 wt%.

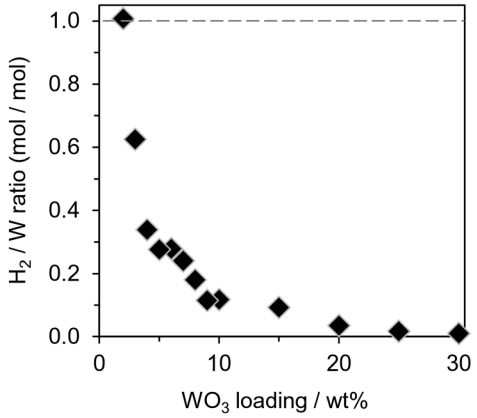

Fig. 11 H_2/W ratio of $Pt/WO_3/Al_2O_3$ catalysts with various WO_3 loadings.

amount of H_2 consumption due to the reduction of Pt species at Pt/Al_2O_3 (45 μmol g^{-1}). Fig. 10(B) shows $X(A)_{WO_3}$; the value decreased with an increase in WO_3 loading. This result suggests that WO_3 loading should affect the reduction property of WO_3. Furthermore, to obtain the degree of WO_3 reduction, the ratio of the H_2 consumption amount due to supported tungsten species (H_2/W ratio) was also estimated as (2)

$$H_2/W \text{ ratio} = X(A)_{WO_3}/N(A) \quad (2)$$

N(A) represents the amount of WO_3 loading. The H_2/W ratios were less than 1 regardless of WO_3 loading (Fig. 11). These results indicate that tungsten species were partially reduced at a temperature region of around 373 K to 573 K except for the catalyst with 2 wt% WO_3 loading. Li and coworkers reported a difference in reducibility between the edge and interior of FeO islands on Pt. FeO at the edge of islands is reduced through the oxidation of benzyl alcohol to benzaldehyde.[73] In our case, tungsten species at the edge of a domain should be exposed to different environmental conditions than that inside of a WO_3 domain. W species at the edge of a domain was deduced to be reduced at lower temperature than that at the inside of a WO_3 domain. Therefore, we can assume that H_2 consumption in the region of 373 K to 573 K is due to the reduction of W species at the perimeter interface between a 2D WO_3 monolayer domain and γ-Al_2O_3.

If the 2D WO_3 monolayer domain possesses a square shape that consists of "n" pieces of WO_6 units on each side, "n" can be estimated by using (3).

$$H_2/W \text{ ratio} = \frac{\text{Number of } WO_6 \text{ units at perimeter } (4n-4)}{\text{Number of total } WO_6 \text{ units } (n^2)} \quad (3)$$

The cross-sectional area of a WO_6 unit that is loaded as a monolayer on a γ-Al_2O_3 surface was reported to be 0.47 nm^2.[72,74] Moreover, the side length of the WO_6 unit is estimated to be 0.22 nm from the square root of the cross-sectional area of the WO_6 unit (Fig. 12). Furthermore, eqn (4)

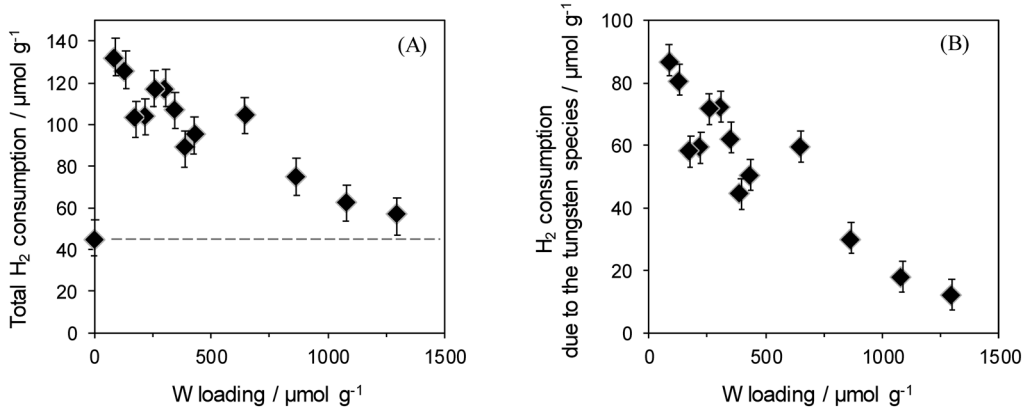

Fig. 10 H_2 consumption of $Pt/WO_3/Al_2O_3$ catalysts with various WO_3 loadings for (A) total amount and (B) the amount due to the tungsten species.

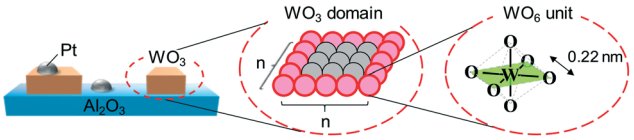

Fig. 12 Structural models of a WO_3 monolayer domain on $Pt/WO_3/Al_2O_3$ catalysts.

gives the length of the perimeter interface between a 2D WO_3 monolayer domain and γ-Al_2O_3:

$$\text{Length of perimeter interface} = \text{Side length of a } WO_6 \text{ unit } (0.22\ \text{nm}) \times \text{Number of } WO_6 \text{ units at the perimeter } (4n - 4) \quad (4)$$

An increase in WO_3 loading decreased the length of the perimeter interface between WO_3 and γ-Al_2O_3 (Fig. 13). These results suggest that small WO_3 domains are highly dispersed on a γ-Al_2O_3 surface in catalysts with a low loading level of WO_3. In contrast, an increase in WO_3 loading causes an increase in size and aggregation of each domain, which leads to a decrease in the number of WO_6 units at the domain edge. Structural analyses of the catalysts based on X-ray spectroscopy revealed that the γ-Al_2O_3 surface was almost fully covered with a 2D WO_3 monolayer domain in the catalyst with 20 wt% WO_3 loading. Therefore, no perimeter interface between WO_3 and γ-Al_2O_3 exists and the perimeter interface length of $Pt/WO_3/Al_2O_3$ catalysts is constant above 20 wt% WO_3 loading (Fig. 14).

Fig. 15 shows the relationship between the perimeter interface length between a 2D WO_3 monolayer domain and γ-Al_2O_3 and the yield of 1,3-propanediol in the hydrogenolysis of glycerol over $Pt/WO_3/Al_2O_3$ catalysts. The positive correlation between the two different parameters indicates that the W–Al perimeter interface plays an important role in the selective hydrogenolysis of glycerol to 1,3-propanediol. A Brønsted acid site is well known to be generated on the bridging bond of a supported metal oxide and its support.[17,18] The active site of this reaction should be a W–(OH)–Al site at the perimeter interface between the WO_3 domain and γ-Al_2O_3. Protonation of the secondary OH of glycerol is promoted by a W–(OH)–Al site, followed by dissociation of the C–O bond at the second position of glycerol and the formation of 1,3-propanediol. Although $Pt/WO_3/Al_2O_3$ catalysts with low WO_3 loading (2–3 wt%) have a large W–Al perimeter interface, the catalytic activity is quite low. This result implies that isolated T_d tungsten species on γ-Al_2O_3 cannot generate the W–(OH)–Al site which acts as an active site for the present reaction.

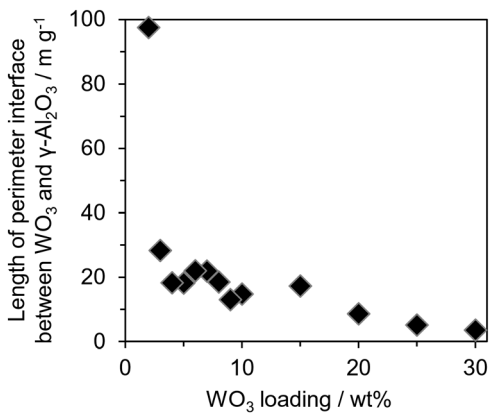

Fig. 13 Effect of WO_3 loading on the perimeter interface between WO_3 and γ-Al_2O_3.

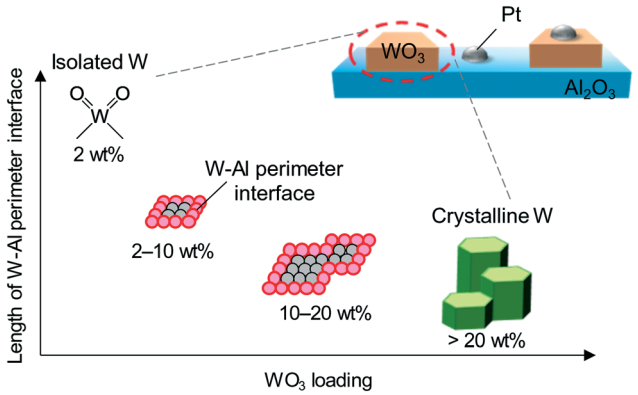

Fig. 14 Models of W species on $Pt/WO_3/Al_2O_3$ catalysts.

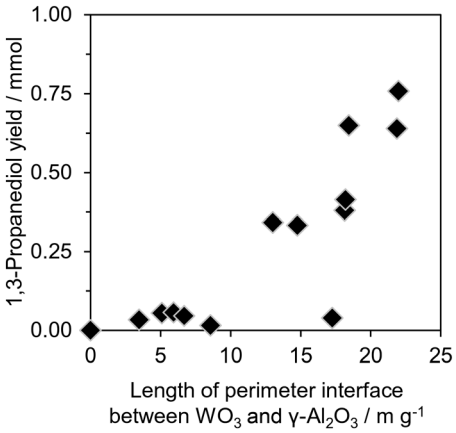

Fig. 15 Effect of the perimeter interface length between WO_3 and γ-Al_2O_3 on hydrogenolysis over $Pt/WO_3/Al_2O_3$ catalysts.

Conclusions

The relationship between the structure of W species on $Pt/WO_3/Al_2O_3$ catalysts and their activities for the selective hydrogenolysis of glycerol to 1,3-propanediol was investigated. Structural analysis of the catalysts based on X-ray spectroscopy indicated that a 2D WO_3 monolayer domain was loaded on the surface of γ-Al_2O_3. H_2-TPR profiles of $Pt/WO_3/Al_2O_3$ catalysts suggested the presence of two kinds of tungsten species with different reducing properties. The tungsten species at the edge of a WO_3 domain was reduced more easily than that inside of a WO_3 domain. Furthermore,

H_2-TPR can estimate the length of the perimeter interface between a 2D WO_3 monolayer domain and γ-Al_2O_3. This revealed a positive correlation between the length of the W–Al perimeter interface and the catalytic activity of $Pt/WO_3/Al_2O_3$ catalyst for the hydrogenolysis of glycerol to 1,3-propanediol. This result indicated that the W–(OH)–Al site at the perimeter interface between a WO_3 domain and γ-Al_2O_3 plays an important role for the hydrogenolysis of glycerol to form 1,3-propanediol.

Conflicts of interest

There are no conflicts to declare.

Acknowledgements

This study was partially supported by the Program for Elements Strategy Initiative for Catalysts & Batteries (ESICB). This work was also supported in part by Grants-in-Aid for Scientific Research (B) (Grant 17H03459) and Scientific Research on Innovative Areas (Grant 17H06443) commissioned by MEXT of Japan. The XAFS experiments at SPring-8 were conducted with the approval (No. 2018A1647) of the Japan Synchrotron Radiation Research Institute (JASRI).

Notes and references

1 H. Hattori, *Appl. Catal., A*, 2015, **504**, 103–109.
2 H. Nair, M. J. Liszka, J. E. Gatt and C. D. Baertsch, *J. Phys. Chem. C*, 2008, **112**, 1612–1620.
3 S. L. Soled, G. B. McVicker, L. L. Murrell, L. G. Sherman, N. C. Dispenziere, S. L. Hsu and D. Waldman, *J. Catal.*, 1988, **111**, 286–295.
4 T. Yamamoto, Y. Tanaka, T. Matsuyama, T. Funabiki and S. Yoshida, *J. Phys. Chem. B*, 2001, **105**, 1908–1916.
5 M. Hino and K. Arata, *J. Chem. Soc., Chem. Commun.*, 1988, 1259–1260.
6 A. H. Karim, S. Triwahyono, A. A. Jalil and H. Hattori, *Appl. Catal., A*, 2012, **433–434**, 49–57.
7 R. W. Gosselink, D. R. Stellwagen and J. H. Bitter, *Angew. Chem., Int. Ed.*, 2013, **52**, 5089–5092.
8 Y. Liu, C. Luo and H. Liu, *Angew. Chem., Int. Ed.*, 2012, **51**, 3249–3253.
9 R. Foo, T. Vazhnova, D. B. Lukyanov, P. Millington, J. Collier, R. Rajaram and S. Golunski, *Appl. Catal., B*, 2015, **162**, 174–179.
10 M. Kantcheva, M. Milanova and S. Mametsheripov, *Catal. Today*, 2012, **191**, 12–19.
11 S. Kwon, P. Deshlahra and E. Iglesia, *J. Catal.*, 2018, **364**, 228–247.
12 J. Macht, T. Carr and E. Iglesia, *J. Am. Chem. Soc.*, 2009, **131**, 6554–6565.
13 K. Chen, A. T. Bell and E. Iglesia, *J. Catal.*, 2002, **209**, 35–42.
14 C. D. Baertsch, S. L. Soled and E. Iglesia, *J. Phys. Chem. B*, 2001, **105**, 1320–1330.
15 D. G. Barton, S. L. Soled, G. D. Meitzner, G. A. Fuentes and E. Iglesia, *J. Catal.*, 1999, **181**, 57–72.
16 E. Iglesia, D. G. Barton, S. L. Soled, S. Miseo, J. E. Baumgartner, W. E. Gates, G. A. Fuentes and G. D. Meitzner, *Stud. Surf. Sci. Catal.*, 1996, **101**, 533–542.
17 I. E. Wachs, *Colloids Surf., A*, 1995, **105**, 143–149.
18 M. A. Vuurman, D. J. Stufkens, A. Oskam and I. E. Wachs, *J. Mol. Catal.*, 1992, **76**, 263–289.
19 W. Zhou, N. Soultanidis, H. Xu, M. S. Wong, M. Neurock, C. J. Kiely and I. E. Wachs, *ACS Catal.*, 2017, **7**, 2181–2198.
20 W. Zhou, E. I. Ross-Medgaarden, W. V. Knowles, M. S. Wong and I. E. Wachs, *Nat. Chem.*, 2009, **1**, 722–728.
21 W. Lin, A. A. Herzing, C. J. Kiely and I. E. Wachs, *J. Phys. Chem. C*, 2008, **112**, 5942–5951.
22 E. I. Ross-Medgaarden, W. V. Knowles, T. Kim, M. S. Wong, W. Zhou, C. J. Kiely and I. E. Wachs, *J. Catal.*, 2008, **256**, 108–125.
23 I. E. Wachs, Y. Chen, J.-M. Jehng, L. E. Briand and T. Tanaka, *Catal. Today*, 2003, **78**, 13–24.
24 I. E. Wachs, *Catal. Today*, 1996, **27**, 437–455.
25 A. M. Turek and I. E. Wachs, *J. Phys. Chem.*, 1992, **96**, 5000–5007.
26 T. Kitano, T. Shishido, K. Teramura and T. Tanaka, *Catal. Today*, 2014, **226**, 97–102.
27 T. Kitano, T. Shishido, K. Teramura and T. Tanaka, *ChemPhysChem*, 2013, **14**, 2560–2569.
28 T. Kitano, T. Shishido, K. Teramura and T. Tanaka, *J. Phys. Chem. C*, 2012, **116**, 11615–11625.
29 T. Shishido, T. Kitano, K. Teramura and T. Tanaka, *Top. Catal.*, 2010, **53**, 672–677.
30 T. Shishido, T. Kitano, K. Teramura and T. Tanaka, *Catal. Lett.*, 2009, **129**, 383–386.
31 T. Kitano, S. Okazaki, T. Shishido, K. Teramura and T. Tanaka, *Catal. Today*, 2012, **192**, 189–196.
32 T. Kitano, S. Okazaki, T. Shishido, T. Teramura and T. Tanaka, *Catal. Lett.*, 2011, **40**, 1332–1334.
33 T. Kitano, S. Okazaki, T. Shishido, T. Teramura and T. Tanaka, *J. Mol. Catal. A: Chem.*, 2013, **371**, 21–28.
34 T. Kitano, T. Hayashi, T. Uesaka, T. Shishido, K. Teramura and T. Tanaka, *ChemCatChem*, 2014, **6**, 2011–2020.
35 R. A. Sheldon, *Green Chem.*, 2014, **16**, 950–963.
36 A. M. Ruppert, K. Weinberg and R. Palkovits, *Angew. Chem., Int. Ed.*, 2012, **51**, 2564–2601.
37 M. Pagliaro and M. Rossi, *The Future of Glycerol*, RSC Publishing, Cambridge, 2008.
38 A. Corma, S. Iborra and A. Velty, *Chem. Rev.*, 2007, **107**, 2411–2502.
39 Y. Nakagawa, Y. Tamura and K. Tomishige, *Res. Chem. Intermed.*, 2018, **44**, 3897–3903.
40 K. Tomishige, Y. Nakagawa and M. Tamura, *Green Chem.*, 2017, **19**, 2876–2924.
41 Y. Nakagawa, M. Tamura and K. Tomishige, *J. Mater. Chem. A*, 2014, **2**, 6688–6702.
42 J. ten Dam and U. Hanefeld, *ChemSusChem*, 2011, **18**, 1017–1034.
43 C. H. Zhou, J. N. Beltramini, Y. X. Fan and G. Q. Lu, *Chem. Soc. Rev.*, 2008, **37**, 527–549.
44 J. ten Dam and U. Hanefeld, *ChemCatChem*, 2013(5), 497–505.

45 R. Arundhathi, T. Mizugaki, T. Mitsudome, K. Jitsukawa and K. Kaneda, *ChemSusChem*, 2013, **6**, 1345–1347.
46 T. Mizugaki, T. Yamakawa, R. Arundhathi, T. Mitsudome, K. Jitsukawa and K. Kaneda, *Chem. Lett.*, 2012, **41**, 1720–1722.
47 T. Kurosaka, H. Maruyama, I. Naribayashi and Y. Sasaki, *Catal. Commun.*, 2008, **9**, 1360–1363.
48 S. García-Fernández, I. Gandarias, J. Requies, F. Soulimani and P. L. Arias, *Appl. Catal., B*, 2017, **204**, 260–271.
49 S. García-Fernández, I. Gandarias, J. Requies, M. B. Güemez, S. Bennici and P. L. Arias, *J. Catal.*, 2015, **323**, 65–75.
50 T. Aihara, H. Kobayashi, S. Feng, H. Miura and T. Shishido, *Chem. Lett.*, 2017, **46**, 1497–1500.
51 S. Feng, A. Nagao, T. Aihara, H. Miura and T. Shishido, *Catal. Today*, 2018, **303**, 207–212.
52 J. Y. Park, L. R. Baker and G. A. Somorjai, *Chem. Rev.*, 2015, **115**, 2781–2817.
53 M. Cargnello, V. V. T. Doan-Nguyen, T. R. Gordon, R. E. Diaz, E. A. Stach, R. J. Gorte, P. Fornasiero and C. B. Murray, *Science*, 2013, **341**, 771–773.
54 H. Yoshida, Y. Kuwauchi, J. R. Jinschek, K. Sun, S. Tanaka, M. Kohyama, S. Shimada, M. Haruta and S. Takeda, *Science*, 2012, **335**, 317–319.
55 E. I. Papaioannou, C. Bachmann, J. J. Neumeier, D. Frankel, H. Over, J. Janek and I. S. Metcalfe, *ACS Catal.*, 2016, **6**, 5865–5872.
56 H. Ariga, T. Taniike, H. Morikawa, R. Tero, H. Kondoh and Y. Iwasawa, *Chem. Phys. Lett.*, 2008, **454**, 350–354.
57 T. F. Jaramillo, K. P. Jørgensen, J. Bonde, J. H. Nielsen, S. Horch and I. Chorkendorff, *Science*, 2007, **317**, 100–102.
58 T. Varga, A. P. Wilkinson, A. C. Jupe, C. Lind, W. S. Bassett and C.-S. Zha, *Phys. Rev. B: Condens. Matter Mater. Phys.*, 2005, **72**, 024117.
59 H. Asakura, S. Yamazoe, T. Misumi, A. Fujita, T. Tsukuda and T. Tanaka, *Radiat. Phys. Chem.*, 2019, DOI: 10.1016/j.radphyschem.2019.04.020.
60 V. I. Nefedov, Y. V. Salyn, G. Leonhardt and R. A. Scheibe, *J. Electron Spectrosc. Relat. Phenom.*, 1977, **10**, 121–124.
61 M. C. Peignon, C. Cardinaud and G. A. Turban, *J. Electrochem. Soc.*, 1993, **140**, 505–512.
62 L. Salvati, L. E. Makovsky, J. M. Stencel, F. R. Brown and D. H. J. Hercules, *J. Phys. Chem.*, 1981, **85**, 3700–3707.
63 S. Yoshida, T. Tanaka, T. Hanada, T. Hiraiwa, H. Kanai and T. Funabiki, *Catal. Lett.*, 1992, **12**, 277–286.
64 H. Yoshida, T. Tanaka, T. Yoshida, T. Funabiki and S. Yoshida, *Catal. Today*, 1996, **28**, 79–89.
65 T. Yamamoto, A. Orita and T. Tanaka, *X-Ray Spectrom.*, 2008, **37**, 226–231.
66 S. Yamazoe, Y. Hitomi, T. Shishido and T. Tanaka, *J. Phys. Chem. C*, 2008, **112**, 6869–6879.
67 J. A. Horsley, I. E. Wachs, J. M. Brown, G. H. Via and F. D. Hardcastle, *J. Phys. Chem.*, 1987, **91**, 4014–4020.
68 K. Kinoshita, K. Routsus and J. A. S. Bett, *Thermochem. Acta*, 1974, **10**, 109–117.
69 J. Barbier, D. Bahloul and P. Marecot, *J. Catal.*, 1992, **137**, 377–384.
70 R. Prins, *Chem. Rev.*, 2012, **112**, 2714–2738.
71 S. Khoobiar, *J. Phys. Chem.*, 1964, **68**, 411–412.
72 A. Martínez, G. Prieto, M. A. Arribas, P. Concepción and J. F. Sánchez-Royo, *J. Catal.*, 2007, **248**, 288–302.
73 G. Zhao, F. Yang, Z. Chen, Q. Liu, Y. Ji, Y. Zhang, Z. Niu, J. Mao, X. Bao, P. Hu and Y. Li, *Nat. Commun.*, 2017, **8**, 14039.
74 C. Pfaff, M. J. P. Zurita, C. Scott, P. Patiño, M. R. Goldwasser, J. Goldwasser, F. M. Mulcahy, M. Houalla and D. M. Hercules, *Catal. Lett.*, 1997, **49**, 13–16.